



**HAL**  
open science

## New kinematic constraints of the western Doruneh fault, northeastern Iran, from interseismic deformation analysis

Giuseppe Pezzo, Cristiano Tolomei, Simone Atzori, Stefano Salvi, Esmail Shabanian, Olivier Bellier, Yassaman Farbod

### ► To cite this version:

Giuseppe Pezzo, Cristiano Tolomei, Simone Atzori, Stefano Salvi, Esmail Shabanian, et al.. New kinematic constraints of the western Doruneh fault, northeastern Iran, from interseismic deformation analysis. *Geophysical Journal International*, 2012, 190 (1), pp.622-628. 10.1111/j.1365-246X.2012.05509.x . hal-01882015

**HAL Id: hal-01882015**

**<https://hal.science/hal-01882015>**

Submitted on 8 Nov 2021

**HAL** is a multi-disciplinary open access archive for the deposit and dissemination of scientific research documents, whether they are published or not. The documents may come from teaching and research institutions in France or abroad, or from public or private research centers.

L'archive ouverte pluridisciplinaire **HAL**, est destinée au dépôt et à la diffusion de documents scientifiques de niveau recherche, publiés ou non, émanant des établissements d'enseignement et de recherche français ou étrangers, des laboratoires publics ou privés.



Distributed under a Creative Commons Attribution 4.0 International License

# New kinematic constraints of the western Doruneh fault, northeastern Iran, from interseismic deformation analysis

Giuseppe Pezzo,<sup>1</sup> Cristiano Tolomei,<sup>1</sup> Simone Atzori,<sup>1</sup> Stefano Salvi,<sup>1</sup>  
Esmaeil Shabanian,<sup>2</sup> Olivier Bellier<sup>2</sup> and Yassaman Farbod<sup>2</sup>

<sup>1</sup>Istituto Nazionale di Geofisica e Vulcanologia, Via di Vigna Murata, 605, 00143 Rome, Italy. E-mail: giuseppe.pezzo@ingv.it

<sup>2</sup>CEREGE, UMR 7330 Aix-Marseille Université and CNRS, Institut Pytheas Technopole Environnement Arbois, Méditerranée, Domaine du Petit Arbois, Avenue Louis Philibert, Les Milles-Aix en Provence BP80, 13545 Aix en Provence, Cedex 04, France

Accepted 2012 April 17. Received 2012 April 13; in original form 2011 August 3

## SUMMARY

We used the SBAS DInSAR analysis technique to estimate the interseismic deformation along the western part of the Doruneh fault system (DFS), northeastern Iran. We processed 90 ENVISAT images from four different frames from ascending and descending orbits. Three of the ground velocity maps show a significant interseismic signal. Using a simple dislocation approach we model 2-D velocity profiles concerning three InSAR data set relative to the western part of the DFS, obtaining a good fit to the observations. The resulting model indicates that a slip rate of  $\sim 5 \text{ mm yr}^{-1}$  accumulates on the fault below 10 km depth, and that in its western sector the Doruneh fault is not purely strike-slip (left-lateral) as in its central part, but shows a significant thrust component. Based on published geological observations, and assuming that all interseismic deformation is recovered with a single event, we can estimate a characteristic recurrence interval between 630 and 1400 yr.

**Key words:** Image processing; Satellite geodesy; Seismic cycle; Radar interferometry; Seismicity and tectonics; Continental tectonics: strike-slip and transform.

## 1 INTRODUCTION AND TECTONIC FRAMEWORK

The Doruneh fault system (DFS) is one of the longest and more prominent faults in Iran (Wellman 1966; Farbod *et al.* 2011). This strike-slip fault system crosses northeastern Iran for about 400 km from the eastern Dasht-e Kavir basin to the Iran–Afghanistan border (Fig. 1a). The DFS system plays an important role in the tectonics of northeastern Iran. It is thought to accommodate part of the  $15 \text{ mm yr}^{-1}$  N–S right-lateral shear observed across Central Iran and the Lut block (Vernant *et al.* 2004; Fattahi *et al.* 2007). In particular, the available geodetic data for northeastern Iran (Vernant *et al.* 2004; Reilinger *et al.* 2006) show a  $\sim 7 \text{ mm yr}^{-1}$  shear rate between the Lut block, south of the DFS and Eurasia (Figs 1a and b). The amount of deformation accumulated on the DFS, as well as the characteristics of its release, are not yet clear, given the scarcity of geodetic, geomorphologic and palaeoseismic data. For this reason the knowledge of the seismotectonics of the fault, is rather limited. Only few moderate ( $M_w$  5–5.8) instrumental earthquakes have been recorded around the entire DFS, whereas the historical record shows no more than one event possibly associated to the DFS. Such low seismicity might be either because of the lack of historical data or

to long recurrence intervals for the largest earthquakes (Ambraseys & Melville 1982; Fattahi *et al.* 2007; Farbod *et al.* 2011).

Geomorphological studies of faulted quaternary deposits along the central DFS trace (Figs 1b and c) show several 10 m of left-lateral displacement in the Holocene (Fattahi *et al.* 2007), from which a long-term slip rate of  $2.5 \text{ mm yr}^{-1}$  is estimated. Recent geomorphological studies (Farbod *et al.* 2011) proposed a model for the DFS, defining three distinct segments characterized by different kinematic regime: the western fault zone (WFZ), the central fault zone (CFZ) and the eastern fault zone (EFZ; Fig. 1b). Although the EFZ displays an imbricate reverse fault zone and NW–SE oriented folding, the CFZ shows exclusively a left-lateral strike-slip motion. The WFZ (Fig. 1b) shows instead evidences of a transpressional local tectonics in agreement with the kinematics of the NE-trending, branching Dahan-Qaleh left-lateral strike-slip fault (DQF in Fig. 1c) and of the NNW–SSE Khartouran reverse fault (KF in Fig. 1c), which terminates the DFS system to the west.

No detailed geodetic measurements are available for the area, and the few existing GPS sites (Vernant *et al.* 2004) are too sparse to be used for a local scale analysis of the interseismic velocity field. A GPS velocity field has been reconstructed by Tavakoli (2007) for Eastern Iran, using survey-mode GPS sites; the two stations

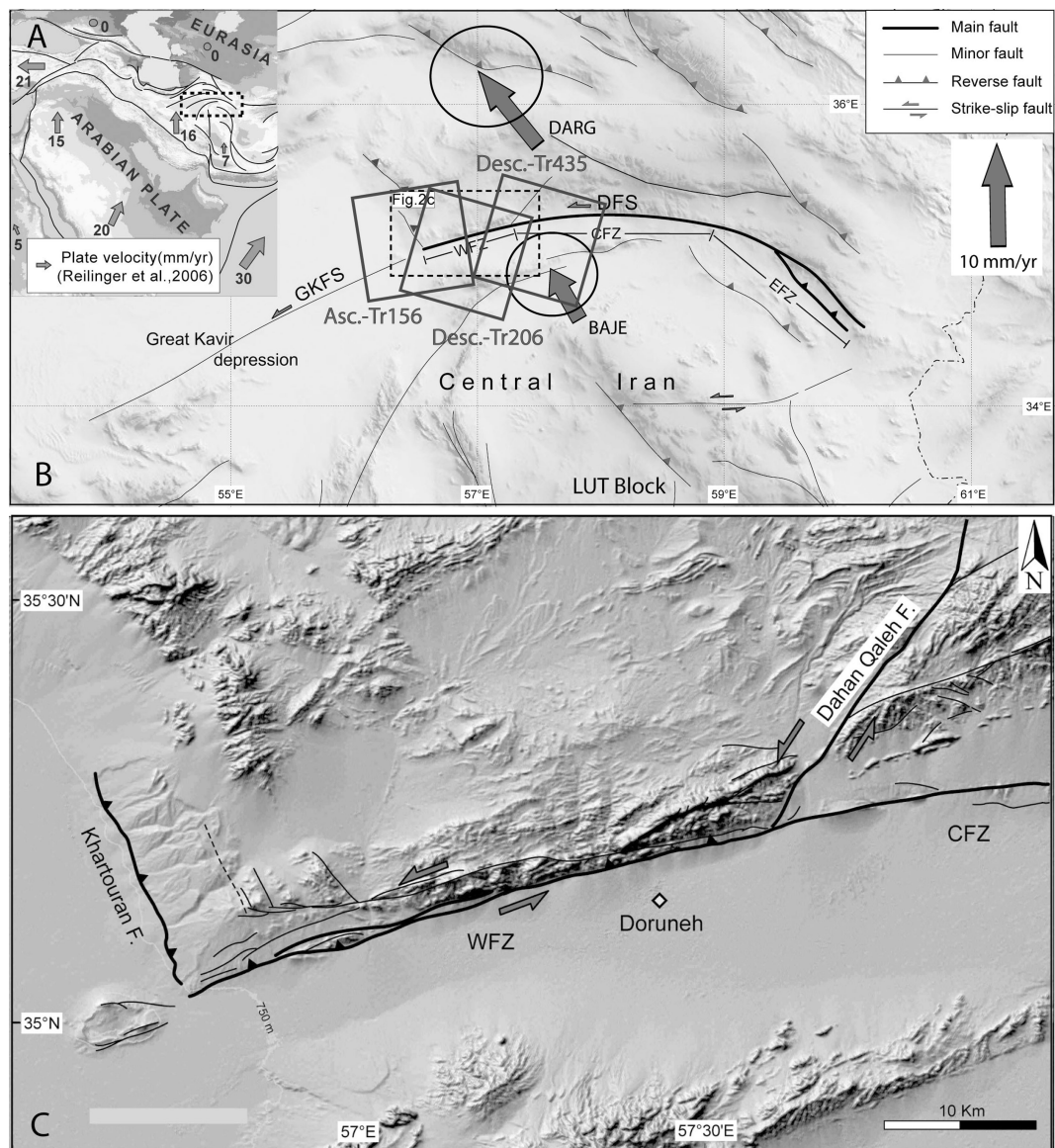


**Figure 1.** (A) Location and geodynamical setting of the Arabia–Eurasia collision zone. Fault mapping results from the Farbod’s PhD thesis work (e.g. Farbod *et al.* 2011). The arrows show plate velocities ( $\text{mm yr}^{-1}$ ) after Reilinger *et al.* (2006) (B) GTOPO30 topographic image on northern part of Central Iran showing the location of the DFS. The arrows show velocities ( $\text{mm yr}^{-1}$ ) of the DARG and BAJE GPS sites (Tavakoli 2007); the three quadrangles show the footprints of the ENVISAT scenes. GKFS, Great Kavir fault system; DFS, Doruneh fault system; WFZ, western fault zone; CFZ, central fault zone, EFZ, eastern fault zone, DQF, Dahan-Qaleh fault; KF, Khartouran fault. (C) Shaded relief map (SRTM) of the WFZ. The trace of the WFZ joins at DQF and KF at its eastern and western terminations, respectively. The KF absorbs the relative westward motion (left-lateral faulting) of WFZ’s northern block by reverse faulting. Left-lateral faulting along the DQF fault implies a prominent reverse component to the left-lateral WFZ.

closer to the WFZ (DARG and BAJE) show a differential left-lateral velocity of  $2.5 \pm 2 \text{ mm yr}^{-1}$ , although they seem to indicate extension across the DFS of  $2.4 \text{ mm yr}^{-1}$ , which contrasts with the geodynamic setting.

In this work, we present the results of interseismic deformation measurement and analysis, carried out using multitemporal differential SAR interferometry (InSAR). We used the InSAR–Small Baseline Subset technique (SBAS) technique (Berardino *et al.* 2002) to process several tens of ENVISAT-ASAR images covering the WFZ with a temporal span of 8 yr, from 2003 to 2010. We calculated the ground velocities over the most coherent areas and modelled the data to investigate the WFZ slip rate and kinematics.

## 2 MULTITEMPORAL INSAR DATA ANALYSIS

We calculated ground displacement time-series and mean ground velocities in the line of sight (LOS), that is, the ground-satellite direction, using the SBAS, developed by Berardino *et al.* (2002).

We processed four ENVISAT-ASAR image mode data sets, acquired from four different frames (Table 1) covering the WDF area. For ascending track, 385 only eight images were available and although this data set was processed, the final velocity was considered too noisy and was not used for subsequent modelling. Using as constraints a maximum normal baseline of

**Table 1.** Multitemporal InSAR data sets. The last three columns indicate the removed residual orbital ramps (see text for explanation).

Data set	Track	Frame	$N^\circ$ of images	Time span	Best-fitting residual orbital ramps		
					Gradient	Strike	Angle with WFZ strike
Asc.	156	692	25	2004–2010	0.08 mm km <sup>-1</sup>	140°	70°
Asc.	385	692	8	2003–2010	n.d.	n.d.	n.d.
Desc.	206	2902	19	2003–2010	0.17 mm km <sup>-1</sup>	15°	55°
Desc.	435	2902	38	2003–2010	0.13 mm km <sup>-1</sup>	27°	43°

300 m and a maximum temporal separation of 1200 d, we generated 79 interferograms for track 156, 52 for track 206 and 113 for track 435. We used the post-processed precise Delft orbits (<http://www.deos.tudelft.nl/ers/precors/>) during interferogram generation, and a  $20 \times 4$  multilooking, to obtain a square pixel with a ground resolution of 80 m. For topographic corrections we used the SRTM-3 Digital Elevation Model (<http://www2.jpl.nasa.gov/srtm/>). The coherence threshold for pixel selection was 0.75. The resulting mean velocity maps are shown in Fig. S1. By averaging, we then reduced the ground resolution to 400 m pixel<sup>-1</sup>, to improve the signal-to-noise ratio and masked the strong subsidence signals observed in the large plain south of the DFS, related to water table overpumping because of agriculture developments (Fig. S1; Anderssohn *et al.* 2008).

InSAR time-series processing results are usually affected by residual orbital signals, not completely removed from the single interferograms during the stack inversion (Biggs *et al.* 2006; Casu *et al.* 2006; Manzo *et al.* 2011). These signals have the same characteristics of interseismic signals: low wavelengths and low rates, and thus need to be modelled and removed before any interseismic modelling. Where possible, this is best accomplished using independent deformation measurements obtained from GPS data (Burgmann *et al.* 2006; Fialko 2006; Manzo *et al.* 2011). Because we did not have enough GPS data to estimate the geodetic signal across the Doruneh fault, we estimated best-fitting linear ramps directly from our velocity maps. The best way to estimate the actual orbital residuals would be to consider an area where there is no tectonic signal. Although it is probably not possible to find an area completely devoid of tectonic deformation in Central Iran, because we are interested in the interseismic deformation accumulating along the Doruneh fault, we first estimated the ramps using velocities located at least 30–40 km from the WFZ trace. Because these estimates might be influenced by a reduced number of data samples, we then compared these ramps to those calculated using the full velocity maps.

For a nearly vertical, mainly strike-slip fault as the WFZ, we expect that the interseismic signal shows the largest variations perpendicularly to the fault (Biggs *et al.* 2006; Fialko 2006; Elliott *et al.* 2008). If the actual residual orbital phase gradients are much steeper, and are oriented at high angles from the expected signal 'ramp', the estimated ramp should contain only a small fraction of interseismic signal. Indeed the differences between the ramps estimated locally and on the entire map were very small: a few degrees in direction and a virtually identical gradient (only for track 156 there is a difference of 0.04 mm yr<sup>-1</sup> km<sup>-1</sup>), confirming the robustness of the estimates. We then subtracted the estimated ramps from the velocity maps, assuming only a small fraction of tectonic signal to have been removed in this process. The final velocity maps are shown in Figs 2(a)–(c). We also ruled out the presence of evident topography-correlated atmospheric artefacts because the correlation with ground velocity is  $\sim 0$ .

The SBAS algorithm does not estimate the uncertainty of the derived mean velocities (Casu *et al.* 2006), and no other geodetic data were available at the same scale. We expect the average uncertainty to be  $\pm 1$  mm yr<sup>-1</sup>, based on the SBAS assessment study by Casu *et al.* (2006).

We observe a clear pattern of accumulation of interseismic deformation across the WFZ. The velocity maps show predominantly higher LOS velocities north of the fault, with a relative difference of  $\sim 2$  mm yr<sup>-1</sup> over a distance of 30–40 km from the fault (Figs 2a and c). There is no clear discontinuity in the velocities across the fault trace, suggesting that no surface creep is presently acting on the WFZ. Two ENVISAT data sets (Figs 2a and c) show velocity patterns with approximate wavelengths of 30–40 km across the fault.

### 3 INTERSEISMIC DEFORMATION MODELLING

We investigated some of the characteristics of the Doruneh fault by a 2-D non-linear modelling of our geodetic observations. Such a simplified model implies that the deformation is constant along strike. Our velocities show a low-varying signal along strike for the two descending data sets, at least up to the DQF intersection to the east. The ascending data set shows instead a  $\sim 3$  mm yr<sup>-1</sup> decrease along the northern side of the DFS, from east to west (Fig. 2). This behaviour is compatible with the presence of a fault discontinuity, and in fact the western limit of the WFZ, as defined by Farbod *et al.* (2011), is here limited by the transversal KF. To avoid any border effect, we inverted only data averaged over box profiles calculated for the central part of the WFZ (Figs 2a–c). We used the three most reliable velocity maps (Table 1), considering their actual LOS, and all weighted equally.

We assume that the WFZ can be approximated by an infinitely long dislocation occurring on a defined fault plane extending from the surface to an infinite depth. The model assumes that the fault part extending below a certain depth is freely slipping and is loading the brittle, upper crustal layer, which is locked in the interseismic period (Savage & Burford 1973). The deformation rates observed at the surface are inverted to retrieve a set of fault parameters at depth. The locking depth is determined by the thickness of the brittle seismogenic layer, where elastic deformation dominates (Savage & Burford 1973). When modelling interseismic deformation across large areas, the presence of parallel faults and across-strike variations of crust rigidity may complicate the deformation pattern up to a point where simple elastic models cannot provide a reasonable fit to the data (Fialko 2006). Although no information exist on possible crust rigidity variations in the area, the presence of a nearly parallel,  $\sim 100$ -km-long fault to the south of the WFZ, bordering to the north of the Dasht-e-Kavir basin, is reported (Fattahi *et al.* 2007). North of the WFZ there are no major mapped faults, but the presence

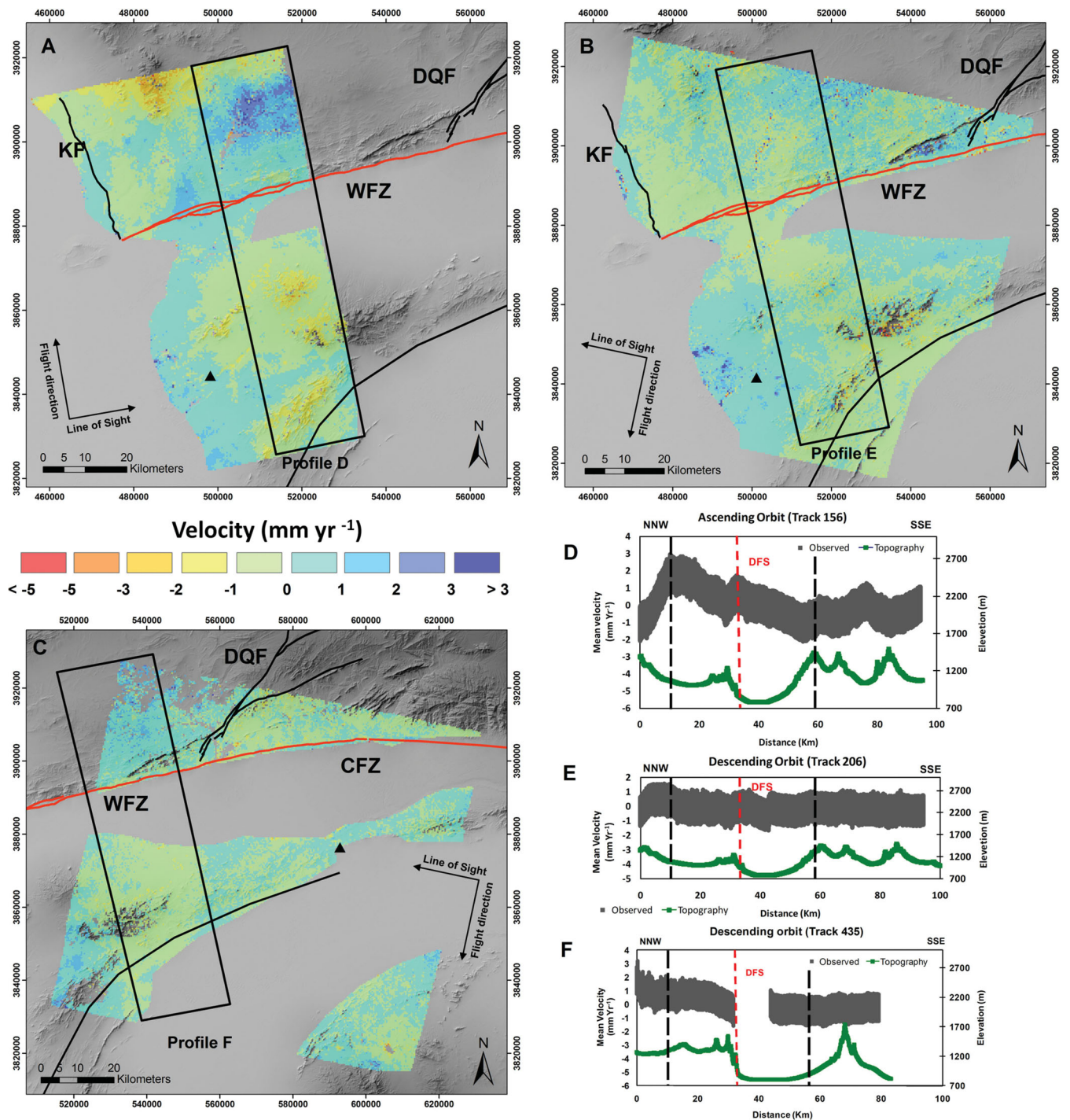


**Figure 2.** Mean LOS velocity maps from (A) ascending track 156, (B) descending track 206 and (C) descending track 435. Positive velocity values (blue colours) indicate ground movement toward the satellite along the LOS direction (inclined  $23^\circ$  from the vertical), negative ones (red colours) indicate the opposite. In red we show the DFS system trace; other faults in the region are in black. Black triangles indicate the reference point; black boxes mark the  $\sim 20$  km buffered velocity profiles reported with the profile (D), (E) and (F), where the topography is also reported in green; dashed red lines mark the intersection with the DFS trace, whereas dashed black lines mark the truncation of profile, around the DFS trace, used in the inversion processing. We show velocity error bars of  $\pm 1$  mm yr $^{-1}$ . All the maps are geo-referenced in UTM WGS84, Zone 40 N.

of ENE–WSW basins and ridges and sharp geological boundaries suggests that a similarly oriented active fault is present here too, at a distance of  $\sim 40$  km. To minimize the possible contributions of interseismic crustal velocities from these nearby faults, we truncated the profiles at a distance where we expect that the observed signal is attributed to WFZ as shown in Fig. 2.

We fixed the fault location and strike angle as the WFZ, the locking depth to 12 km (average depth of the regional seismicity according to Engdahl *et al.* 2006), and simulated an infinitely long and deep fault. Using the Okada (1985) analytical solutions, we jointly inverted all profiles of the three data sets for the fault dip, rake and slip rate by means of a non-linear, least-squares inversion

algorithm based on the Levenberg–Marquardt approach, as described by Atzori *et al.* (2009); the convention for dip, rake and strike angles is the same as Okada (1985). We used a value of 30 GPa for the Lamé constants. The comparison between observed and predicted data is shown in Fig. 3 for the three velocity maps. We tested also a 15-km-locking depth, obtaining very similar dip and rake and a 20 per cent slip rate increase as shown in Fig. S2. The parameter uncertainty (Fig. 3d) was estimated with 150 restarts of the inversion, adding, each time, a synthetic noise correlated in space according to InSAR data statistical properties (Atzori *et al.* 2008); using this procedure we found that rake and slip are better resolved whereas the dip has a higher uncertainty. We obtained a best-fitting solution with an rms of  $0.6 \text{ mm yr}^{-1}$  for the ascending track 156,  $0.6 \text{ mm yr}^{-1}$  for the descending track 206 and  $0.7 \text{ mm yr}^{-1}$  for the descending track 435. In the Fig. S3 we show the histograms of the residuals velocities (observed-modelled).

According to our modelling procedure, the WFZ fault plane is constrained by the InSAR observations to be north-dipping, with dip values in the interval  $60 \pm 11^\circ$  and that for a locking depth of 12 km, the most probable slip rates are  $5 \pm 1 \text{ mm yr}^{-1}$ . The rake angle defines a left-lateral strike-slip, with a small compressive component (rake between  $30^\circ$  and  $38^\circ$ ), although an anticorrelation between slip and rake is present (Fig. 3d).

#### 4 DISCUSSION AND CONCLUSION

Our simple 2-D model is able to fit the observations quite well (Fig. 3). The inverted model parameters, while confirming the main characteristics of this sector of the DFS, give new information insights into the seismic potential of the fault.

Our model confirms the general left-lateral kinematics of the DFS, as first defined by Wellman (1966), but an additional important thrust component along the WFZ is necessary to fit the observations (rake angle of  $34 \pm 4^\circ$ ). The modelled rake angle results in the left-lateral component being about 2/3 of the slip rate, which is in agreement with the long term record as reconstructed by structural and geomorphic observations. A steep fault dip to the north ( $\sim 60^\circ$ ) is well constrained by the observations, and is in agreement with field observations on the western and central DFS.

Our modelled slip rate of  $5 \pm 1 \text{ mm yr}^{-1}$  is the first quantitative estimate of strain accumulation for the western DFS, corresponding to  $\sim 4 \text{ mm yr}^{-1}$  of pure horizontal movement (along the fault strike:  $255^\circ$ ). In the long term, Fattahi *et al.* (2007) estimates  $\sim 2.4 \text{ mm yr}^{-1}$  of left-lateral slip rate on the CFZ, by infrared stimulated luminescence dating of one Holocene alluvial fan, at longitude  $58^\circ 10'$ . Although this is so far the only geological slip rate available for the DFS, it cannot be extended to the entire length of the DFS. In fact, there are many geological and geomorphological evidences that the maximum rupture length of a single earthquake along the DFS system is  $\sim 100 \text{ km}$  (Fattahi *et al.* 2007; Farbod *et al.* 2011).

The transpressive character of the WFZ resulting from our model is in agreement with the kinematic model proposed by Farbod *et al.* (2011), in which the slip vector of WFZ is compatible with those of the left-lateral strike-slip DQF and of the reverse KF (Fig. 1c). Indeed the topography along the fault trace is suggesting a long-term uplift of the northern block (Fig. 1). In our model, the anticorrelation between the slip and rake indicates that some vertical component (rake  $> 0$ ) is needed to explain the observations, otherwise the slip rates for pure strike-slip fault would be unrealistic (with respect to the geological estimates). There are no geological

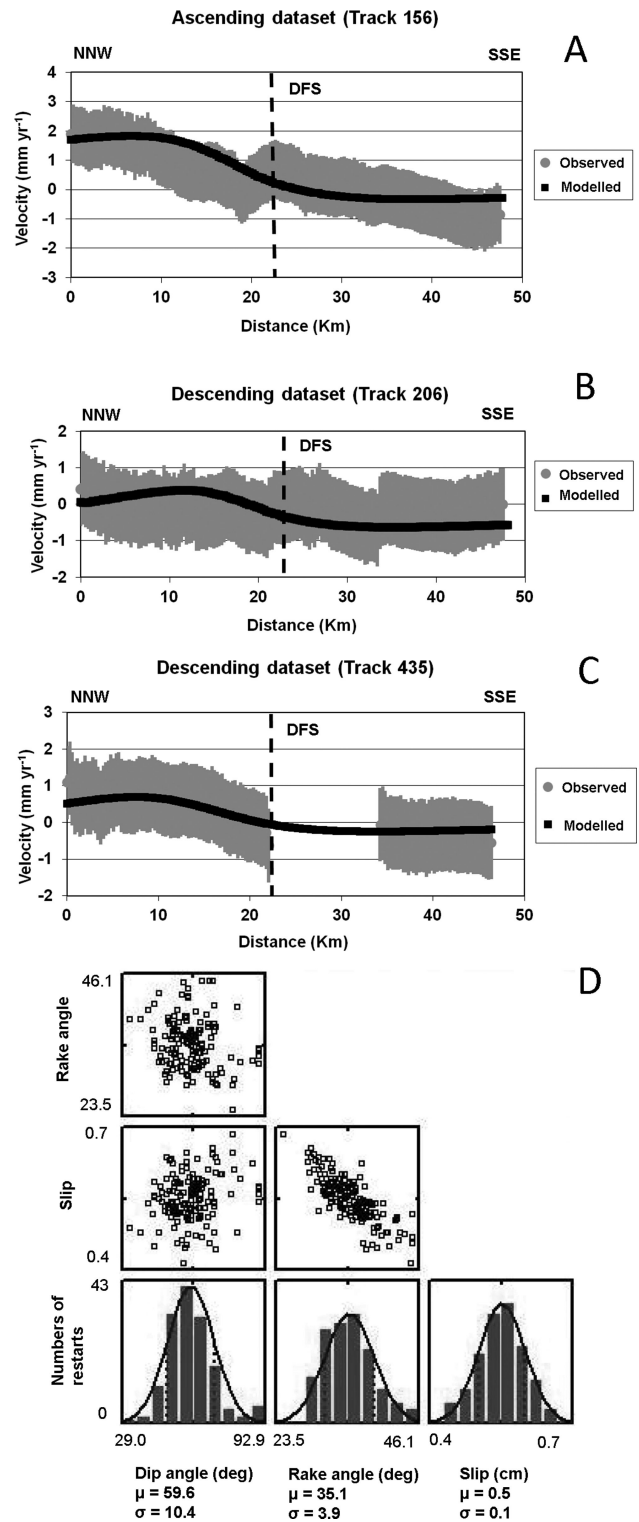


**Figure 3.** Observed (grey) versus modelled (black) velocity profiles for (A) ascending track 156, (B) descending track 206 and (C) descending track 435; dashed lines mark the intersection with the DFS trace. (D) Mean ( $\mu$ ), standard deviation ( $\sigma$ ) and trade-offs of inverted parameters, calculated as described in the text.

estimates of Quaternary uplift rate along the WFZ. Extrapolating the vertical component of our modelled slip rate ( $2.4 \pm 1 \text{ mm yr}^{-1}$ ) in the geological past does not seem to justify the relatively low relief across the WFZ (500–700 m). On the other hand, geological

and geodetic slip rates often show differences (e.g. Fialko 2006; Elliott *et al.* 2008), which could be because of a number of different factors, for example observation and/or model uncertainties, spatio-temporal slip rate variations, interaction with close tectonic structures.

At the regional scale, our slip rate and slip vector for the WFZ are in agreement with the sparse quantitative data available on the present deformation field (Vernant *et al.* 2004). Our model implies a shortening rate across the WFZ of  $\sim 1.3 \text{ mm yr}^{-1}$ , which is 1/4–1/5 of the total shortening accommodated between the Lut block and Eurasia, as measured by GPS networks (Vernant *et al.* 2004). This result implies that other faults with similar rates of activity north of the Lut block accommodate the rest of this shortening.

Based on a geologically determined average slip per event of 4.7 m, the recurrence interval along the Central DFS has been estimated to  $\sim 2000 \text{ yr}$  (Fattahi *et al.* 2007). The slip rate we estimated for the WFZ would require a slip per event of  $\sim 10 \text{ m}$  to obtain the same recurrence time. This is unrealistic, especially if we consider the field observations and the segmentation model by Farbod *et al.* (2011). Accepting for the WFZ a similar slip per event as for the CFZ, including a conservative uncertainty estimate of 20 per cent, we obtain a recurrence interval varying between 630 and 1400 yr. The lack of strong seismicity in the last 1500 yr along the WFZ may be because of the incompleteness of the historical seismic catalogues (Ambraseys & Melville 1982), and our results show that recurrence intervals below 1000 yr cannot be excluded. Localized aseismic deformation (creeping) along the DFS trace may also justify the paucity of strong seismicity (as discussed by Farbod *et al.* 2011), but higher spatial resolution geodetic data would be required to ascertain its presence. Further geomorphological and palaeoseismological investigations will give a more accurate assessment of slip rates, recurrence intervals and relevance of distributed strain mechanisms, providing the means to estimate the seismic hazard along this important active fault.

## ACKNOWLEDGMENTS

This work has been partially carried out under contract with the Agenzia Spaziale Italiana (SIGRIS project). GP was supported by the same project. We thank R. Lanari for providing the SBAS software. ENVISAT images were released under Cat1 project no. 5605. This study was partly carried under the frame of a cooperation agreement that permits to GP to stay in CEREGE during 3 months as visiting PhD student. We thank C. Faccenna for his help and encouragement and J.P. Merryman Boncori for his suggestions on SAR data interpretation.

## REFERENCES

- Ambraseys, N.N. & Melville, C.P., 1982. *A History of Persian Earthquakes*, Cambridge University Press, Cambridge.
- Anderssohn, J., Wetzel, H.U., Walter, T.R., Motagh, M., Djamour, Y. & Kaufmann H., 2008. Land subsidence pattern controlled by old alpine basement faults in the Kashmar Valley, northeast Iran: results from InSAR and levelling, *Geophys. J. Int.*, **174**, 287–294, doi:10.1111/j.1365-246X.2008.03805.x.
- Atzori, S. *et al.*, 2009. Finite fault inversion of DInSAR coseismic displacement of the 2009 L'Aquila earthquake (Central Italy), *Geophys. Res. Lett.*, **36**, 115305, doi:10.1029/2009GL039293.
- Atzori, S., Manunta, M., Fornaro, G., Ganas, A. & Salvi, S., 2008. Post-seismic displacement of the 1999 Athens earthquake retrieved by the differential interferometry by synthetic aperture radar time series, *J. geophys. Res.*, **113**, B09309, doi:10.1029/2007JB005504.
- Berardino, P., Fornaro, G., Lanari, R. & Sansosti, E., 2002. A new algorithm for surface deformation monitoring based on small baseline differential SAR interferograms, *IEEE Trans. Geosci. Remote Sens.*, **40**, 2375–2383.
- Biggs, J., Wright, T., Lu, Z. & Parsons, B., 2007. Multi-interferogram method for measuring interseismic deformation: Denali Fault, Alaska, *Geophys. J. Int.*, **170**, 1165–1179, doi: 10.1111/j.1365-246X.2007.03415.x.
- Burgmann, R., Hilley, G., Ferretti, A. & Novali, F., 2006. Resolving vertical tectonics in the San Francisco Bay Area from permanent scatterer InSAR and GPS analysis, *Geology*, **34**, 221–224.
- Casu, F., Manzo, M. & Lanari, R., 2006. A quantitative assessment of the SBAS algorithm performance for surface deformation retrieval, *Remote Sens. Environ.*, **102**(3–4), 195–210, doi:10.1016/j.rse.2006.01.023.
- Elliott, J.R., Biggs, J., Parsons, B. & Wright, T.J., 2008. InSAR slip rate determination on the Altyn Tagh Fault, northern Tibet, in the presence of topographically correlated atmospheric delays, *Geophys. Res. Lett.*, **35**, L12309, doi:10.1029/2008GL036359.
- Engdahl, E.R., Jackson, J.A., Myers, S.C., Bergman, E.A. & Priestley, K., 2006. Relocation and assessment of seismicity in the Iran region, *Geophys. J. Int.*, **167**, 761–778, doi:10.1111/j.1365-246X.2006.03127.x.
- Farbod, Y., Bellier, O., Shabanian, E. & Abbassi, M.R., 2011. Geomorphic and structural variations along the Doruneh Fault System (central Iran), *Tectonics*, **30**, TC6014, doi:10.1029/2011TC002889.
- Fattahi, M., Walker, R.T., Khatib, M.M., Dolati, A. & Bahroudi, A., 2007. Slip-rate estimate and past earthquakes on the Doruneh fault, eastern Iran, *Geophys. J. Int.*, **168**, 691–709, doi:10.1111/j.1365-246X.2006.03248.x.
- Fialko, Y., 2006. Interseismic strain accumulation and the earthquake potential on the southern San Andreas fault system, *Nature*, **441**, 968–971, doi:10.1038/nature04797.
- Manzo, M., Fialko, Y., Casu, F., Pepe, A. & Lanari, R., 2011. A quantitative assessment of DInSAR measurements of interseismic deformation: the Southern San Andreas Fault case study, *Pure appl. Geophys.*, **1**, 20, doi:10.1007/s00024-011-0403-2.
- Okada, Y., 1985. Surface deformation due to shear and tensile faults in a half-space, *Bull. seism. Soc. Am.*, **75**, 1135–1154.
- Reilinger, R. *et al.*, 2006. GPS constraints on continental deformation in the Africa-Arabia-Eurasia continental collision zone and implications for the dynamics of plate interactions, *J. geophys. Res.*, **111**, B05411, doi:10.1029/2005JB004051.
- Savage, J.C. & Burford, R.O., 1973. Geodetic determination of relative plate motion in central California, *J. geophys. Res.*, **78**, 832–845, doi:10.1029/JB078i005p00832.
- Tavakoli, F., 2007. Present-day kinematics of the Zagros and east of Iran faults, *PhD thesis*, University of Joseph Fourier, Grenoble.
- Vernant, P. *et al.*, 2004. Present-day crustal deformation and plate kinematics in the Middle East constrained by GPS measurements in Iran and northern Oman, *Geophys. J. Int.*, **157**, 381–398, doi:10.1111/j.1365-246X.2004.02222.x.
- Wellman, H.W., 1966. Active wrench faults of Iran, Afghanistan and Pakistan, *Int. J. Earth Sci.*, **55**, 716–735.

## SUPPORTING INFORMATION

Additional Supporting Information may be found in the online version of this article:

**Figure S1.** Original velocity maps obtained from the SBAS process chain on the ascending track 156 data set (A), descending track 206 (C), descending track 435 (E). B, D and E show the corresponding ramps estimated and removed from the original maps.

**Figure S2.** Plots of the correlation between locking depth and slip rate (A), rake angle (B) and dip angle (C). The figure highlights as

no substantial variations of slip rate, dip and rake are present in a reliable interval (10–15 km) of locking depths.

**Figure S3.** Histograms of velocity residuals of the modelled box profile, relative to the ascending track 156 (A), descending track 206 (B) and descending track 435 (C).

Please note: Wiley-Blackwell are not responsible for the content or functionality of any supporting materials supplied by the authors. Any queries (other than missing material) should be directed to the corresponding author for the article.